



ARL-MR-1023 • AUG 2020



# Resolution as a Computational Factor in ALEGRA Simulations of a Shaped Charge Jet: Supplemental Study

by Daniel J Hornbaker

Approved for public release; distribution is unlimited.

## **NOTICES**

### **Disclaimers**

The findings in this report are not to be construed as an official Department of the Army position unless so designated by other authorized documents.

Citation of manufacturer's or trade names does not constitute an official endorsement or approval of the use thereof.

Destroy this report when it is no longer needed. Do not return it to the originator.



# **Resolution as a Computational Factor in ALEGRA Simulations of a Shaped Charge Jet: Supplemental Study**

**Daniel J Hornbaker**

*Weapons and Materials Research Directorate, CCDC Army Research Laboratory*

**REPORT DOCUMENTATION PAGE**

*Form Approved*  
OMB No. 0704-0188

Public reporting burden for this collection of information is estimated to average 1 hour per response, including the time for reviewing instructions, searching existing data sources, gathering and maintaining the data needed, and completing and reviewing the collection information. Send comments regarding this burden estimate or any other aspect of this collection of information, including suggestions for reducing the burden, to Department of Defense, Washington Headquarters Services, Directorate for Information Operations and Reports (0704-0188), 1215 Jefferson Davis Highway, Suite 1204, Arlington, VA 22202-4302. Respondents should be aware that notwithstanding any other provision of law, no person shall be subject to any penalty for failing to comply with a collection of information if it does not display a currently valid OMB control number.

**PLEASE DO NOT RETURN YOUR FORM TO THE ABOVE ADDRESS.**

<b>1. REPORT DATE (DD-MM-YYYY)</b> August 2020		<b>2. REPORT TYPE</b> Memorandum Report		<b>3. DATES COVERED (From - To)</b> May–July 2020	
<b>4. TITLE AND SUBTITLE</b> Resolution as a Computational Factor in ALEGRA Simulations of a Shaped Charge Jet: Supplemental Study				<b>5a. CONTRACT NUMBER</b>	
				<b>5b. GRANT NUMBER</b>	
				<b>5c. PROGRAM ELEMENT NUMBER</b>	
<b>6. AUTHOR(S)</b> Daniel J Hornbaker				<b>5d. PROJECT NUMBER</b> 1L162618AH80	
				<b>5e. TASK NUMBER</b>	
				<b>5f. WORK UNIT NUMBER</b>	
<b>7. PERFORMING ORGANIZATION NAME(S) AND ADDRESS(ES)</b> CCDC Army Research Laboratory ATTN: FCDD-RLW-PE Aberdeen Proving Ground, MD 21005-5069				<b>8. PERFORMING ORGANIZATION REPORT NUMBER</b>  ARL-MR-1023	
<b>9. SPONSORING/MONITORING AGENCY NAME(S) AND ADDRESS(ES)</b>				<b>10. SPONSOR/MONITOR'S ACRONYM(S)</b>	
				<b>11. SPONSOR/MONITOR'S REPORT NUMBER(S)</b>	
<b>12. DISTRIBUTION/AVAILABILITY STATEMENT</b> Approved for public release; distribution is unlimited.					
<b>13. SUPPLEMENTARY NOTES</b> ORCID ID: Daniel J Hornbaker, 0000-0002-0746-1614					
<b>14. ABSTRACT</b> This report follows up on three open questions from a previous study of resolution effects in ALEGRA simulations of a 65-mm shaped charge jet. The underlying cause of fragmented morphology observed in the leading portion of jets at high resolution is investigated. The dependence of the thermodynamic state in the pressure head on temporal discretization is determined. Finally, the accuracy of estimates for resolution-dependent numerical uncertainty is tested against ensembles of randomized simulations at varying resolution.					
<b>15. SUBJECT TERMS</b> numerical simulation, uncertainty quantification, ALEGRA, shaped charge jet, resolution study					
<b>16. SECURITY CLASSIFICATION OF:</b>			<b>17. LIMITATION OF ABSTRACT</b>  UU	<b>18. NUMBER OF PAGES</b>  42	<b>19a. NAME OF RESPONSIBLE PERSON</b> Daniel J Hornbaker
<b>a. REPORT</b> Unclassified	<b>b. ABSTRACT</b> Unclassified	<b>c. THIS PAGE</b> Unclassified			<b>19b. TELEPHONE NUMBER (Include area code)</b> 410-278-7697

## Contents

---

<b>List of Figures</b>	<b>iv</b>
<b>List of Tables</b>	<b>v</b>
<b>Acknowledgments</b>	<b>vi</b>
<b>1. Introduction</b>	<b>1</b>
<b>2. Jet-Tip Morphology</b>	<b>1</b>
<b>3. Jet Temperature</b>	<b>4</b>
<b>4. Ensembles of Randomized Simulations</b>	<b>6</b>
4.1 Method	6
4.2 500- $\mu\text{m}$ Ensemble	7
4.3 500- $\mu\text{m}$ Ensemble sans Maximum Time-Step Control	13
4.4 Ensembles at Multiple Resolutions	14
<b>5. Conclusion</b>	<b>18</b>
<b>6. References</b>	<b>19</b>
<b>Appendix A. Randomly Generated Parameter Values for Simulation Ensembles</b>	<b>20</b>
<b>List of Symbols, Abbreviations, and Acronyms</b>	<b>33</b>
<b>Distribution List</b>	<b>34</b>

## List of Figures

---

Fig. 1	Jet-tip morphology at 40 $\mu\text{s}$ across multiple resolutions in 2-D baseline simulations .....	1
Fig. 2	Jet-tip morphology at 40 $\mu\text{s}$ across multiple resolutions in 2-D simulations with the void insertion model removed .....	2
Fig. 3	Jet-tip morphology at 40 $\mu\text{s}$ across multiple resolutions in 2-D simulations with force fracture off.....	3
Fig. 4	Jet-tip morphology at 40 $\mu\text{s}$ across multiple resolutions in 2-D simulations with the void-insertion minimum volume fraction set to 0.5.....	3
Fig. 5	Jet-tip morphology at 40 $\mu\text{s}$ across multiple resolutions in 2-D simulations with threshold fracture pressure set to $-2.3$ GPa.....	4
Fig. 6	(left) Pressure head temperature and (right) mass average temperature vs. resolution in baseline 2-D simulations .....	5
Fig. 7	(left) Pressure head temperature at 15 $\mu\text{s}$ and (right) mass average temperature at 40 $\mu\text{s}$ vs. maximum time step at two different resolutions .....	5
Fig. 8	Distribution of total liner mass at 40 $\mu\text{s}$ in simulations at 500- $\mu\text{m}$ resolution.....	8
Fig. 9	Total liner mass at 40 $\mu\text{s}$ vs. origin shift in simulations at 500- $\mu\text{m}$ resolution.....	9
Fig. 10	Distribution of total kinetic energy at 40 $\mu\text{s}$ in simulations at 500- $\mu\text{m}$ resolution.....	10
Fig. 11	Distribution of total axial momentum at 40 $\mu\text{s}$ in simulations at 500- $\mu\text{m}$ resolution.....	10
Fig. 12	Distribution of mass average temperature at 40 $\mu\text{s}$ in simulations at 500- $\mu\text{m}$ resolution.....	11
Fig. 13	Total internal energy vs. total mass temperature at 40 $\mu\text{s}$ in simulations at 500- $\mu\text{m}$ resolution.....	11
Fig. 14	Mass average temperature at 40 $\mu\text{s}$ vs. maximum time step in simulations at 500- $\mu\text{m}$ resolution .....	12
Fig. 15	Distribution of mass average temperature at 40 $\mu\text{s}$ in simulations at 500- $\mu\text{m}$ resolution sans maximum time-step control .....	13
Fig. 16	Distribution of total internal energy at 40 $\mu\text{s}$ in simulations at 500- $\mu\text{m}$ resolution sans maximum time-step control .....	14
Fig. 17	Estimated and ensemble values for total kinetic energy at 40 $\mu\text{s}$ vs. resolution.....	14
Fig. 18	Ensemble values relative to estimated mean for total kinetic energy at 40 $\mu\text{s}$ vs. resolution .....	15

Fig. 19	Ensemble values relative to estimated mean for total kinetic energy at 40 $\mu\text{s}$ vs. resolution .....	16
Fig. 20	Ensemble values relative to estimated mean for total kinetic energy at 40 $\mu\text{s}$ vs. resolution .....	16
Fig. 21	Ensemble values relative to estimated mean for total kinetic energy at 40 $\mu\text{s}$ vs. resolution .....	17

## List of Tables

---

Table 1	Estimated mean values and standard deviations for jet properties at 40 $\mu\text{s}$ at multiple resolutions .....	9
Table 2	Comparison of estimated and ensemble mean values and standard deviations for jet properties at 40 $\mu\text{s}$ across multiple resolutions .....	17
Table A-1	Randomized parameter values for the 500- $\mu\text{m}$ -resolution simulation ensemble .....	22
Table A-2	Randomized parameter values for the 500- $\mu\text{m}$ -resolution simulation ensemble with unrestricted time steps .....	25
Table A-3	Randomized parameter values for the 999- $\mu\text{m}$ -resolution simulation ensemble with unrestricted time steps .....	27
Table A-4	Randomized parameter values for the 750- $\mu\text{m}$ -resolution simulation ensemble with unrestricted time steps .....	29
Table A-5	Randomized parameter values for the 250- $\mu\text{m}$ -resolution simulation ensemble with unrestricted time steps .....	31

## **Acknowledgments**

---

This work was performed under the Terminal Ballistics for Lethality and Protection Sciences Frontier Project, and was supported in part by a grant of computer time from the US Department of Defense High Performance Computing Modernization Program at the US Army Combat Capabilities Development Command Army Research Laboratory Department of Defense Supercomputing Resource Center.

## 1. Introduction

---

Resolution effects in ALEGRA simulations of a 65-mm shaped charge jet (SCJ) were recently reported.<sup>1</sup> Further investigation of three topics was suggested: 1) the fragmented structure in the leading portion of high-resolution jets, 2) the dependence of the thermodynamic state in the pressure head on temporal discretization, and 3) the accuracy of estimates concerning resolution-dependent numerical uncertainty. This supplemental work follows through on these suggestions.

The models, methods, and setup from the previous report are retained here, with changes or modifications noted in the text. Two-dimensional simulations are used exclusively throughout, as the prior work indicates good correlation between 2-D and 3-D simulation outcomes. Jet-tip morphology at high resolution is examined in Section 2. The dependence of jet temperature on temporal discretization is investigated in Section 3. The final part of this study compares estimates of resolution-dependent numerical uncertainty against the outcomes of randomized simulation ensembles in Section 4. Concluding remarks are found in Section 5.

## 2. Jet-Tip Morphology

---

Void spaces open along the jet axis in simulations at 200- $\mu\text{m}$  resolution, and the leading portion of the jet takes on an increasingly fragmented structure at finer resolutions (Fig. 1). At 15- $\mu\text{m}$  resolution, a slender continuous core of jet material can be seen encased within a finely fractured network. Such morphologies have not been observed in real jets. Experimental observations of 65-mm SCJ devices show jets having generally smooth, continuous outer profiles with some evidence of a molten liquid core.<sup>2,3</sup>

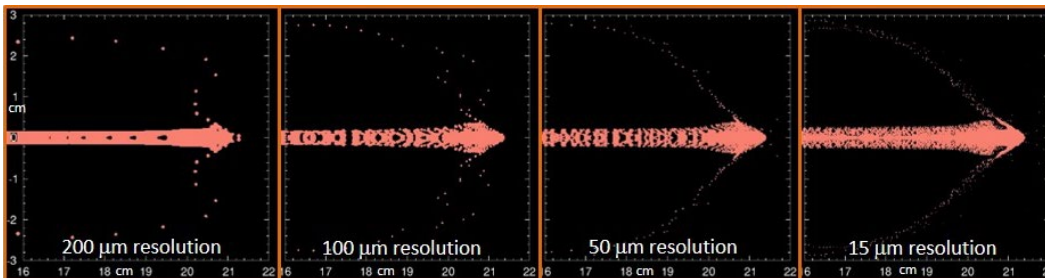


Fig. 1 Jet-tip morphology at 40  $\mu\text{s}$  across multiple resolutions in 2-D baseline simulations

The Mie–Grüneisen equation of state (EOS) used in these simulations does not account for material phase transitions. This may play some role in the excessive fracturing of the jet. Alternate choices of EOS model could produce different

jet-tip morphologies at high resolution. However, selection of material models and their associated parameters has wide-ranging effects on simulation outcomes and is outside the scope of this inquiry.

Another mechanism to consider is material fracture. Since no damage model is used in these simulations, tensile fracture is generated entirely by ALEGRA's void insertion model. This model relieves excessive tensile pressure (which is negative by convention) by allowing the volume of material in a cell to decrease, with a corresponding increase in void space. The default behavior is for pressure to relax to zero over 10 time steps.

Simulations performed with the void insertion model removed show smooth, continuous jet profiles with no voids along the axis (Fig. 2). This indicates that the void insertion model is the cause of the fragmented jet-tip morphology.

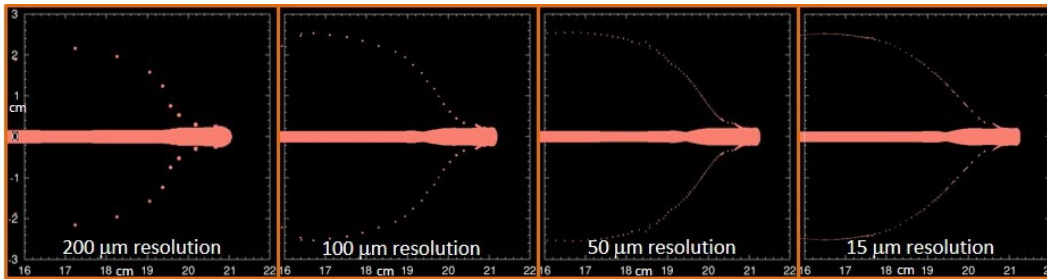


**Fig. 2 Jet-tip morphology at 40  $\mu$ s across multiple resolutions in 2-D simulations with the void insertion model removed**

There are two conditions under which void insertion activates for the copper jet material. The first is a threshold pressure of  $-1.50$  GPa below which the material fractures. A second condition is implemented by turning on the “force fracture” option, which enables a density floor below which the material fractures. This floor is set at  $7.114$  g/cm<sup>3</sup> (80% of the initial copper density) in these simulations.

Simulations performed with force fracture turned off (Fig. 3) show no effect on jet morphology. Simulations at 200-, 100-, and 50- $\mu$ m resolution are mathematically identical to the baseline simulations, meaning the force fracture condition is never met in these cases. At 15- $\mu$ m resolution, the first evidence of divergence from the baseline configuration occurs around  $32.19$   $\mu$ s (about 53,860 cycles), but the impact on jet-tip morphology is negligible. This rules out density rarefaction as a factor in jet fragmentation at high resolution.

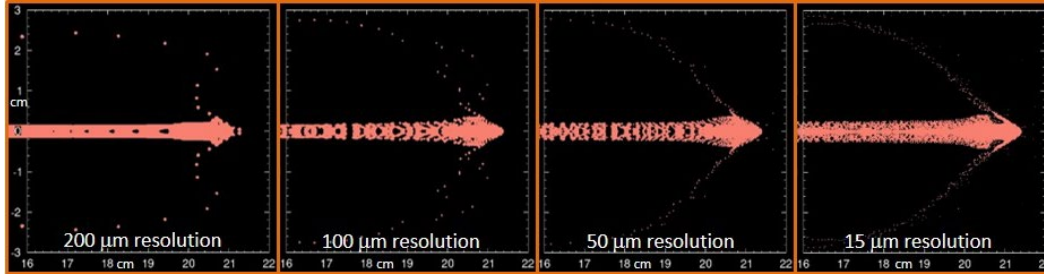


**Fig. 3 Jet-tip morphology at 40  $\mu$ s across multiple resolutions in 2-D simulations with force fracture off**

One additional void insertion model parameter is the minimum volume fraction. This sets a cell occupancy limit below which the void insertion model is not applied. The baseline configuration used the code default value of 1E-9. Simulations were run with the minimum volume fraction increased to 0.5 (Fig. 4). While this changed specific details of the fragmentation patterns, the general morphology remained consistent with that seen in the baseline configuration.

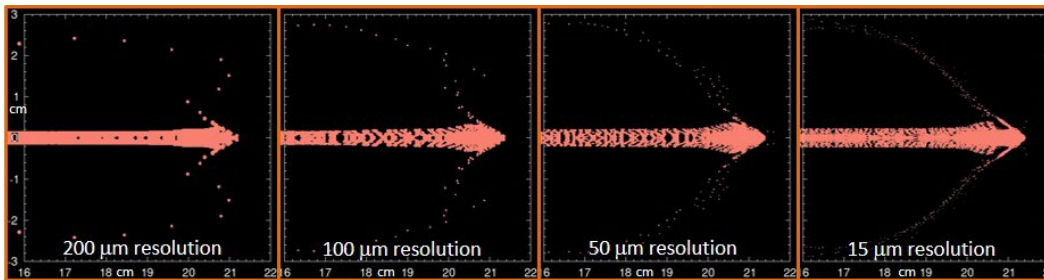


**Fig. 4 Jet-tip morphology at 40  $\mu$ s across multiple resolutions in 2-D simulations with the void-insertion minimum volume fraction set to 0.5**

The remaining factor is the threshold fracture pressure. The baseline configuration value of  $-1.50$  GPa is taken from Kmetyk et al.<sup>4</sup> Other sources suggest a value of  $-2.30$  GPa for the fracture pressure of copper.<sup>5</sup> In simulations using this value (Fig. 5), axial voids no longer appear at 200- $\mu$ m resolution, but fragmentation persists at 100- and 50- $\mu$ m resolution. Intriguingly, at 15- $\mu$ m resolution the jet tip is once again fully solid. Not observable in the 15- $\mu$ m resolution image is a moderate amount of exterior fragmentation below the 16-cm axial position, but a solid continuous central core spans the full length of the jet.

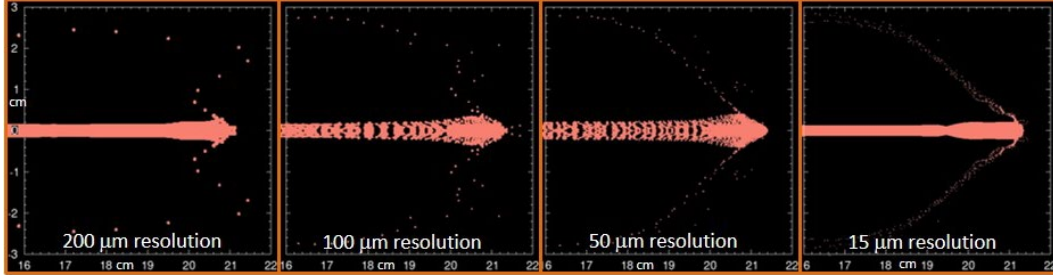


**Fig. 5** Jet-tip morphology at 40  $\mu$ s across multiple resolutions in 2-D simulations with threshold fracture pressure set to  $-2.3$  GPa

Considering that simulations without the void insertion model are functionally equivalent to setting the threshold fracture pressure to  $-\infty$ , it is fair to surmise that further lowering the threshold fracture pressure parameter will eventually eliminate jet-tip fragmentation at resolutions below 200  $\mu$ m. However, adjusting material parameter values to obtain desired results in simulations is generally not recommended. There is enough latitude in computational codes to obtain a wide range of behaviors in any particular simulation. Changing parameter values based on outcomes raises the risk of getting the “right” answer for the wrong reasons, and such simulations may not correspond with reality. A better practice is to independently determine material model parameters from unrelated materials characterization testing. Uncertainty quantification techniques can be applied to investigate any unexpected simulation outcomes that may subsequently arise.

An interesting possibility suggested by the trends seen in Figs. 1 and 5 is that jet-tip fragmentation may be transient with resolution. Numerical estimation of modeled physical processes depends closely on the spatial and temporal grids used, which is a major point of the previous report and this supplement. The observed jet fragmentation is consistent with pressures reaching maximum tension at some resolution between 200 and 15  $\mu$ m. The progression in morphology in Fig. 5 shows fragmentation restricted within a limited range of resolution, while in the baseline simulations of Fig. 1 the onset of a solid core at 15  $\mu$ m suggests that fragmentation is beginning to lessen with increasing refinement.

### 3. Jet Temperature

---

The temperature of a simulated jet generally decreases with increasingly fine resolution. This is reflected in the thermodynamic state of the material at the pressure head. As shown in Fig. 6, decreasing cell size lowers the temperature in the pressure head, which in turn results in a cooler jet.

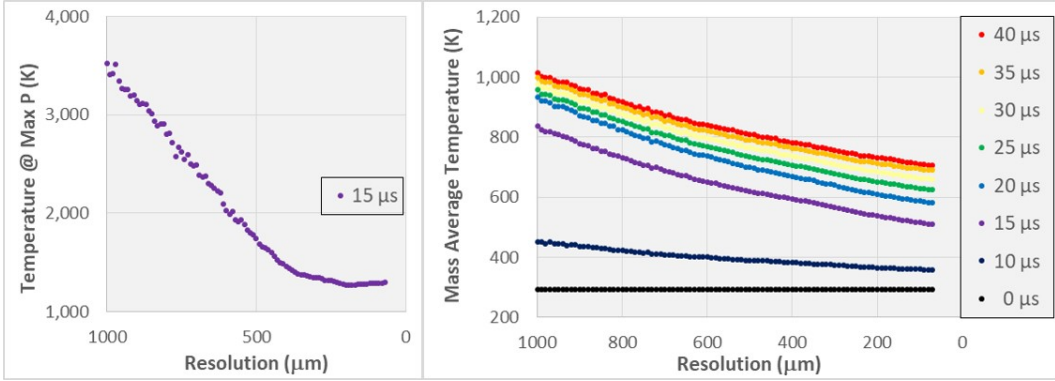


**Fig. 6 (left) Pressure head temperature and (right) mass average temperature vs. resolution in baseline 2-D simulations**

One consequence of decreasing cell size is a reduction in time-step duration to satisfy numerical stability criteria. A natural question is whether the resolution-dependent temperature decrease in the pressure head is due primarily to spatial or temporal effects. This can be probed by limiting the allowed size of time steps in simulations at fixed resolution.

In baseline simulations, the maximum time step  $t_{max}$  was set to 0.001 s, which is functionally unlimited, as time steps were always much shorter. Simulations were run at 999- and 500- $\mu\text{m}$  resolutions with  $t_{max}$  set as low as 1 ns (Fig. 7). At 999- $\mu\text{m}$  resolution, the simulation with  $t_{max} = 100$  ns was mathematically identical to the baseline simulation, meaning all time steps in the baseline simulation were less than this value. The same is true at 500- $\mu\text{m}$  resolution for  $t_{max} = 50$  ns.

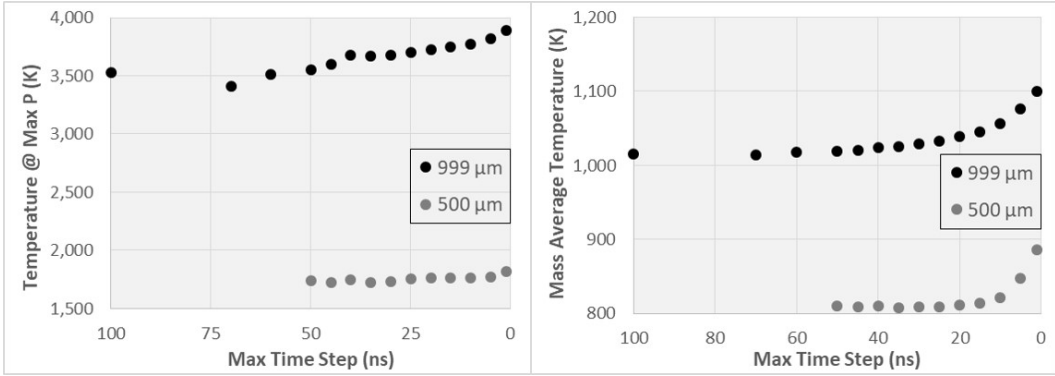


**Fig. 7 (left) Pressure head temperature at 15  $\mu\text{s}$  and (right) mass average temperature at 40  $\mu\text{s}$  vs. maximum time step at two different resolutions**

The pressure head temperature, and subsequently the mass average temperature  $\bar{T}$  of the jet, generally increases with decreasing  $t_{max}$  at fixed resolution. The logical conclusion is that the spatial effect on pressure head temperature must be much greater than the temporal effect as resolution is made increasingly fine.

The  $\bar{T}$  data are well fit by a function of the form

$$\bar{T} = A e^{-\frac{t_{max}}{b}} + C \quad (1)$$

Some thought is required concerning which data points to fit. In baseline simulations there is some longest time step  $t_+$ , generally at or near the beginning of the simulation when most of the material is static. For any value of  $t_{max}$  longer than  $t_+$ , the resulting simulation will be mathematically identical to the baseline simulation, and  $\bar{T}$  will remain constant:

$$\bar{T}(t_{max} \geq t_+) = A e^{-\frac{t_+}{b}} + C \quad (2)$$

An additional consideration is the case in which  $t_{max}$  is shorter than  $t_+$  but longer than the shortest baseline time step  $t_-$ , which typically occurs at or near the end of a simulation. In this mixed regime, some time steps will be limited to  $t_{max}$ , while others will be shorter. In contrast, when  $t_{max}$  is less than  $t_-$ , all simulation time steps are limited, resulting in a uniform temporal grid.

Uniform temporal grids were seen at  $t_{max} \leq 60$  ns in 999- $\mu\text{m}$ -resolution simulations, and  $t_{max} \leq 20$  ns at 500- $\mu\text{m}$  resolution. Data fits including the mixed regime were very similar to those limited to just the uniform case. Fit parameters for the uniform case were  $A = 86.21$  K,  $b = 13.23$  ns, and  $C = 1018.36$  K for the 999- $\mu\text{m}$ -resolution data, and  $A = 93.79$  K,  $b = 5.42$  ns, and  $C = 808.50$  K at 500- $\mu\text{m}$  resolution. The root mean square errors for these fits were 1.68 and 1.53 K. Setting  $t_{max} = 0$  in Eq. 1 provides an estimate of  $\bar{T} = A + C$  in the limit of continuous time, with a value of 1104.6 K at 999- $\mu\text{m}$  resolution and 902.3 K at 500- $\mu\text{m}$  resolution.

## 4. Ensembles of Randomized Simulations

---

A fundamental aim of the previous study was quantifying the distribution of outcomes related to purely computational factors in simulations of the model SCJ system. A method for estimating the expected mean value and distribution widths for jet properties as a function of resolution was conjectured. This method is now put to the test by comparing estimates with distributions of outcomes from ensembles of simulations with randomly generated computational parameters.

### 4.1 Method

---

Five computational factors were initially selected for randomization, four of which are related to the structure of the computational domain. A quick review of computational domain structure in baseline simulations is helpful.

Two-dimensional simulations employ a cylindrical coordinate system with the  $x$ -axis corresponding to the radial direction and the  $y$ -axis being the axis of rotational symmetry. The end of the SCJ liner is initially positioned at the coordinate origin in the baseline configuration, and the device is oriented so that the jet advances in the positive  $y$  direction. The maximum coordinate value  $x_{\max}$  was set to the smallest value over 60 mm commensurate with an integer number of cells,

$$x_{\max}^{(2-D)} = r * \text{ceiling}(60/r) \quad (3)$$

where  $r$  is the resolution in millimeters. The coordinate limits along the  $y$  axis were calculated similarly, with the included axial lengths on either side of the origin being 140 and 240 mm:

$$y_{\min}^{(2-D)} = -r * \text{ceiling}(140/r) \quad (4)$$

$$y_{\max}^{(2-D)} = r * \text{ceiling}(240/r) \quad (5)$$

The coordinate origin is always coincident with a mesh node in the baseline simulation domain structure.

Simulation parameters were randomized within the previously established automated workflow using the Python `random.randint()` function, which implements the Mersenne Twister pseudorandom number generator.<sup>6</sup>

Domain size was randomly increased in each of the three allowed directions (radial, and both axial directions) by an integer number of cells up to a maximum distance of 25 mm. The maximum time step was set to an integer number of nanoseconds from 1 to 46. The coordinate origin was shifted by integer number of microns from 0 to 1 less than the simulation resolution by subtracting this distance from  $y_{\min}^{(2-D)}$ .

Lists of the randomly generated parameter values for simulation ensembles are provided in the Appendix.

## 4.2 500- $\mu\text{m}$ Ensemble

---

The first ensemble generated consisted of 100 simulations at 500- $\mu\text{m}$  resolution. Values for the five randomized parameters are listed in Table A-1 of the Appendix.

Analysis begins with a check for mass loss by comparing total liner mass at 0 and 40  $\mu\text{s}$ . Mass loss can occur from mass flowing beyond domain boundaries and material discards. Additionally, mass can vanish by falling below the minimum volume fraction of 1E-16 recognized by code, but such losses fall far below the measurement precision of 0.0001 g used in this work. Mass loss directly affects

extensive jet properties such as total kinetic energy and is a type of variation undesirable in this investigation. Six simulations had mass losses of 0.0001 g, an amount considered negligible. Throughout the rest of this work only one additional simulation exhibited mass loss, also at the measurement precision limit.

Total liner mass ranges from 79.0790 to 79.2769 g in this ensemble. The distribution is shown in Fig. 8, with data binned in 0.025-g intervals and the first bin in the figure centered at 79.0 g. The MATLAB implementation of the Anderson–Darling test<sup>7</sup> indicates the data are not consistent with a normal distribution, with a p-value less than the minimum MATLAB tabulated value of 0.0005. The shape of the distribution suggests it may be a sum of two normal distributions with differing means, a type of distribution belonging to a class known as mixture distributions. Anderson–Darling tests on a simple partitioning of the data indicate both the smallest 71 values and largest 29 values are separately consistent with normal distributions, with respective p-values of 0.1657 and 0.1257.

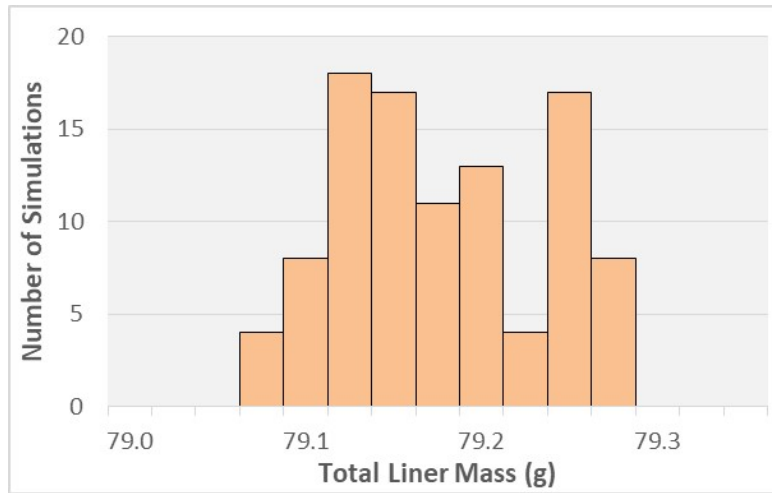


**Fig. 8** Distribution of total liner mass at 40  $\mu$ s in simulations at 500- $\mu$ m resolution

Variations in liner mass arise from origin shifts, which changes the initial positioning of the SCJ model geometry relative to cell boundaries. A plot of total liner mass with origin shift (Fig. 9) supports the conjecture that the data are consistent with a mixture distribution.

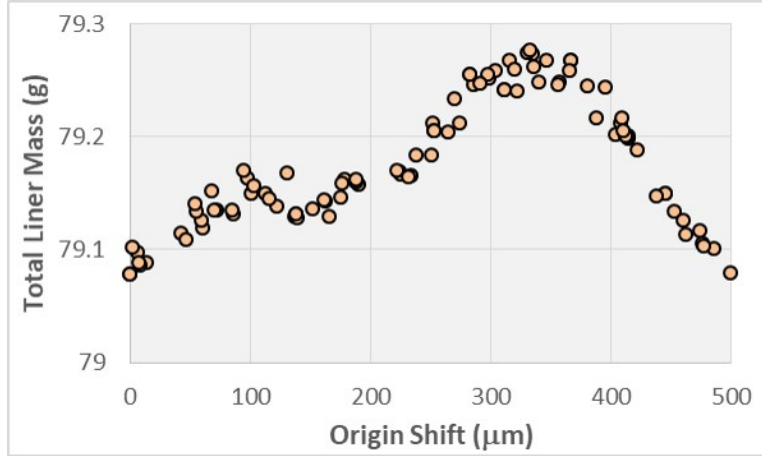


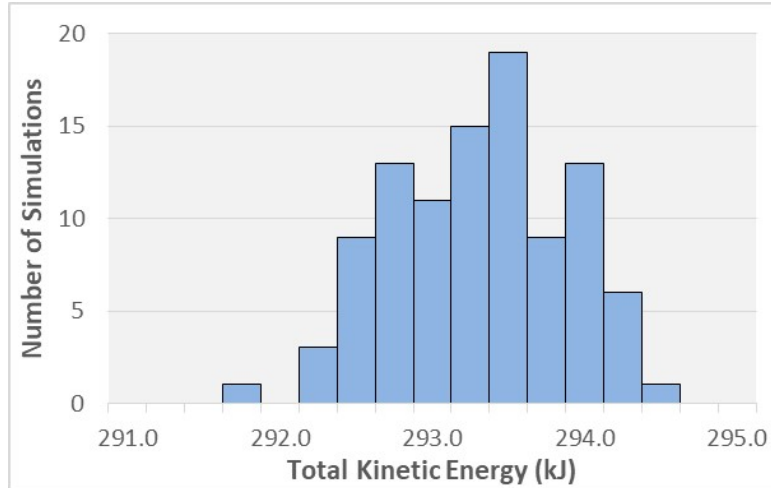
**Fig. 9** Total liner mass at 40 μs vs. origin shift in simulations at 500-μm resolution

Having found that mass losses are essentially negligible, attention now turns to the jet properties whose variations were estimated with respect to resolution in the previous report. Table 1 shows estimated mean values and standard deviations for four jet properties at multiple resolutions.

**Table 1** Estimated mean values and standard deviations for jet properties at 40 μs at multiple resolutions

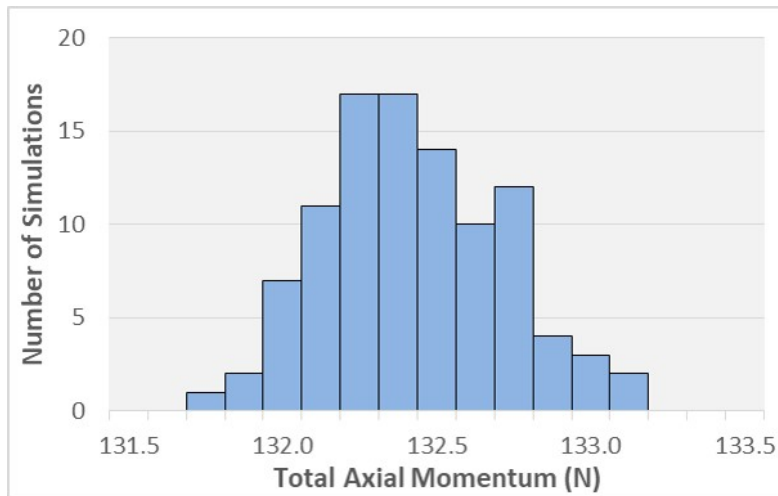
Jet property at 40 μs	999 μm		750 μm		500 μm		250 μm	
	Mean	$\sigma$	Mean	$\sigma$	Mean	$\sigma$	Mean	$\sigma$
Total kinetic energy (kJ)	270.2	1.35	283.1	1.01	294.2	0.68	303.3	0.34
Total axial momentum (N)	131.7	0.98	132.5	0.73	132.6	0.49	132.1	0.24
Mass average temperature (K)	1009.2	6.96	897.9	5.22	808.9	3.48	742.7	1.74
Total internal energy (kJ)	32.8	0.24	29.0	0.18	26.1	0.12	23.9	0.06

The distribution of total kinetic energy for the 500-μm ensemble is displayed in Fig. 10, with 0.250-kJ bin widths and the first bin centered at 291.0 kJ. The data are consistent with a normal distribution (p-value of 0.3123). The mean value of 293.3 kJ is within 1 kJ of the estimate. The standard deviation of the data is 0.56 kJ, somewhat less than the estimated value of 0.68 kJ.



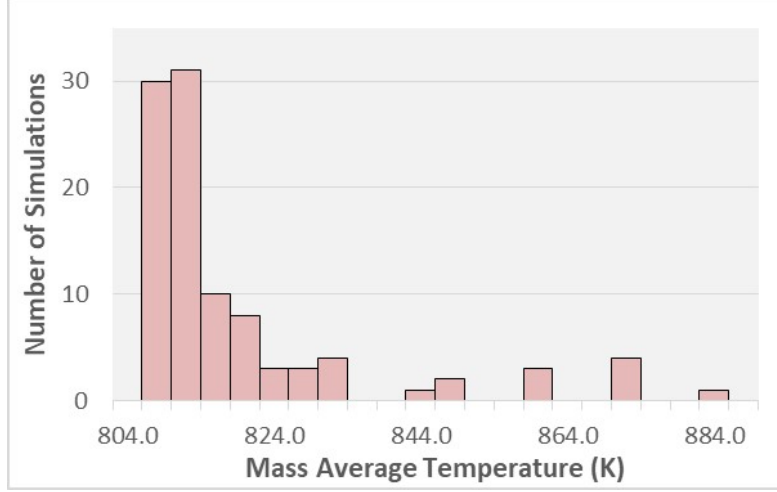
**Fig. 10** Distribution of total kinetic energy at 40  $\mu\text{s}$  in simulations at 500- $\mu\text{m}$  resolution

Figure 11 shows the distribution of total axial momentum, with 0.125-N bin widths and the first bin centered at 131.5 N. The data are again consistent with a normal distribution (p-value of 0.6236). The estimated mean value is very nearly the same as the data mean of 132.4 N. The standard deviation of 0.29 N is only about 60% as wide as the estimated value of 0.49 N.



**Fig. 11** Distribution of total axial momentum at 40  $\mu\text{s}$  in simulations at 500- $\mu\text{m}$  resolution

The distribution of  $\bar{T}$  (Fig. 12) is decidedly not normal, with the Anderson–Darling test returning a p-value  $< 0.0005$ . The data span a relatively broad range of values, from a minimum of 807.5 K to a maximum of 885.0 K at the far end of the long tail.



**Fig. 12** Distribution of mass average temperature at 40  $\mu\text{s}$  in simulations at 500- $\mu\text{m}$  resolution

The distribution of total internal energy mirrors that of  $\bar{T}$ . These quantities are closely correlated over the ensemble, with a plot of total internal energy versus total mass temperature (the product of  $\bar{T}$  and liner mass) being highly linear (Fig. 13).

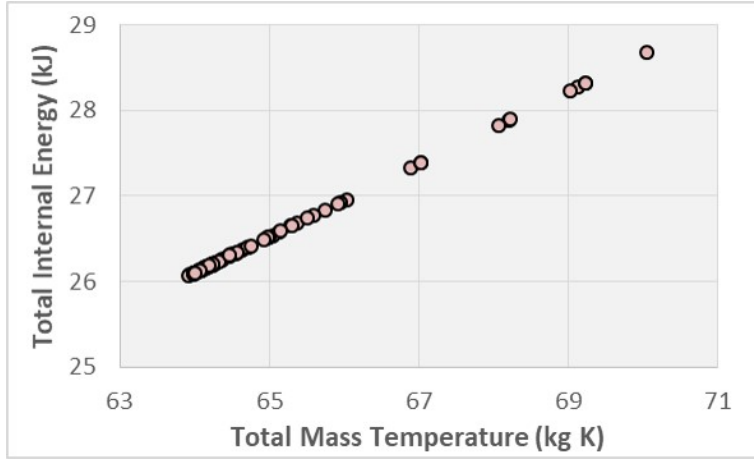


**Fig. 13** Total internal energy vs. total mass temperature at 40  $\mu\text{s}$  in simulations at 500- $\mu\text{m}$  resolution

Keep in mind that this specific correlation only holds over the limited ensemble range at 40  $\mu\text{s}$  and is not universal. While the Mie–Grüneisen EOS is explicitly constructed with internal energy depending linearly on temperature, material density is also a factor. From the previous report, the specific internal energy  $E$  (with units of energy per mass) is given by

$$E = \frac{\chi^2 u_s^2}{2} + \frac{\min(\chi, 0) P_0}{\rho_0} + C_v \left[ T - T_h + T_0 \left( 1 - \frac{[\min(\chi, 0) \Gamma_0]^2}{2} \right) \right] \quad (6)$$

Note this equation corrects an error in Eq. 83 of the previous report, where the *min* functions were mistakenly stated as *max* functions. Density  $\rho$  in this equation is recast as  $\chi$ :

$$\chi \equiv 1 - \frac{\rho_0}{\rho} \quad (7)$$

where  $\rho_0$  is the initial material density. Other quantities in Eq. 6 are the initial pressure  $P_0$ , initial temperature  $T_0$ , Grüneisen parameter  $\Gamma_0$ , shock front velocity  $u_s$ ,

$$u_s = \frac{c_s}{1 - s_1 \max(\chi, 0)}; \quad (\chi < \chi_{hmax}), \quad (8)$$

(with material bulk sound speed  $c_s$  and linear Mie–Grüneisen parameter  $s_1$ ), and the Hugoniot temperature  $T_h$ ,

$$T_h = \begin{cases} e^{\Gamma_0 \chi} T_0 + \frac{\chi^2 u_s^2}{c_v} Y(\chi) & ; \chi \geq 0 \\ (1 + \chi \Gamma_0) T_0 & ; \chi < 0 \end{cases} \quad (9)$$

$$Y(\chi) = \frac{e^{\Gamma_0 \chi}}{\chi^2 u_s^2} \int_0^\chi \frac{\chi^2 u_s(\chi)}{e^{\Gamma_0 \chi}} \frac{du_s(\chi)}{d\chi} d\chi \quad (10)$$

Returning to the distribution for  $\bar{T}$ , the long tail is a direct consequence of the time-step effect on jet temperature uncovered in Section 3. Plotting  $\bar{T}$  against the maximum time step across the ensemble (Fig. 14) returns a plot matching that in Fig. 7. While selection of maximum time step was randomized in the ensemble, and thus consistent with a uniform distribution over the allowed range of values, the effect on jet temperature is far from random, with the exponential dependence of Eq. 1 producing the long tail in the distribution of  $\bar{T}$ .

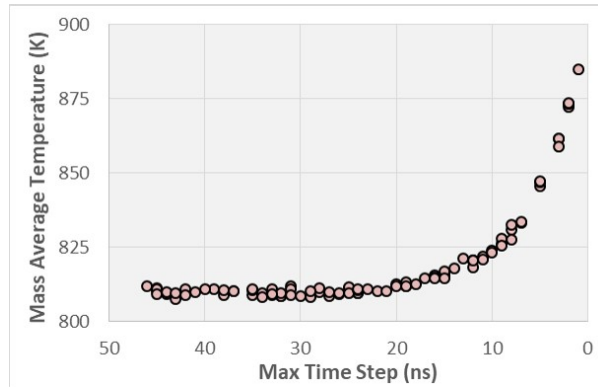


**Fig. 14** Mass average temperature at 40  $\mu\text{s}$  vs. maximum time step in simulations at 500- $\mu\text{m}$  resolution

The simulations used in generating the estimates of mean values and variabilities of jet properties in the previous report did not include maximum time-step limits.

These are rarely employed in general practice. A new ensemble at 500- $\mu\text{m}$  resolution was generated with maximum time-step limitations removed.

### 4.3 500- $\mu\text{m}$ Ensemble sans Maximum Time-Step Control

Values for the four randomized parameters in this ensemble of 100 simulations are listed in Table A-2 of the Appendix.

The mean value of the total kinetic energy is 293.6 kJ with a standard deviation of 0.43 kJ. For the total axial momentum, the mean value is 132.4 N and the standard deviation is 0.33 N. These values are similar to those from the previous ensemble.

Eliminating maximum time-step control removes the tail from the distribution of  $\bar{T}$  (Fig. 15, with 0.25-K bin width and first bin centered at 807.0 K). This distribution is not particularly consistent with normality (p-value of 0.009), but  $\bar{T}$  distributions from the ensembles at 999, 750, and 250  $\mu\text{m}$  discussed in the next section return p-values of 0.253, 0.181, and 0.017, so these distributions are considered “normal enough” for statistical analysis purposes. The ensemble mean value for  $\bar{T}$  is 809.8 K, in line with the estimated value of 808.9. However, the standard deviation of 0.95 K is notably smaller than the estimated value of 3.48 K.

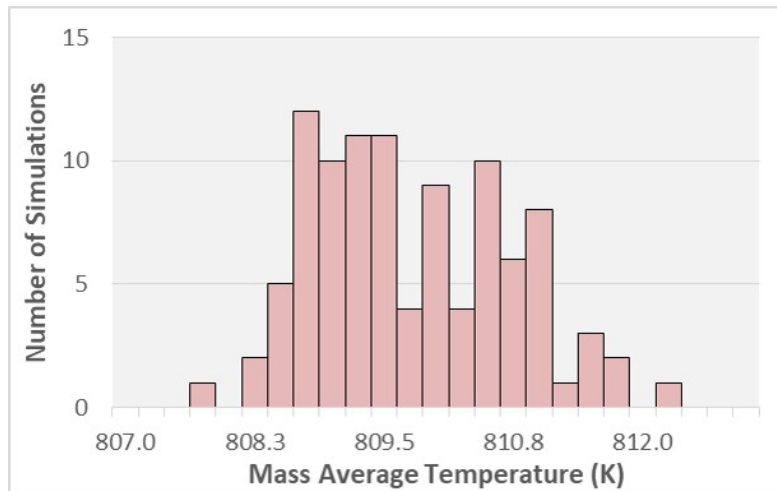


**Fig. 15** Distribution of mass average temperature at 40  $\mu\text{s}$  in simulations at 500- $\mu\text{m}$  resolution sans maximum time-step control

The distribution for total internal energy is shown in Fig. 16, with a 0.01-kJ bin width and the first bin centered at 26.05 kJ. The Anderson–Darling test returns a p-value of 0.758, indicating normality. Values for the mean and standard deviation are 26.1 and 0.04 kJ, respectively. Again, the mean value is consistent with the estimated value, while the standard deviation is somewhat less.

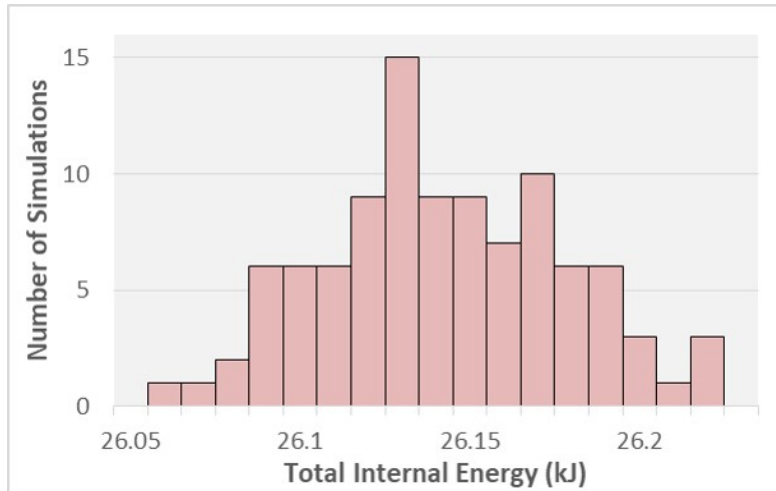


**Fig. 16** Distribution of total internal energy at 40  $\mu$ s in simulations at 500- $\mu$ m resolution sans maximum time-step control

#### 4.4 Ensembles at Multiple Resolutions

Additional ensembles of 100 simulations were generated at 999-, 750-, and 250- $\mu$ m resolution. Values for the four randomized parameters in each ensemble are listed in Tables A-3 through A-5 of the Appendix.

Figure 17 plots the ensemble mean values for total kinetic energy against the estimated mean curve, with error bars indicating the standard deviation of the ensemble distributions and the shaded region representing the estimated standard deviations.

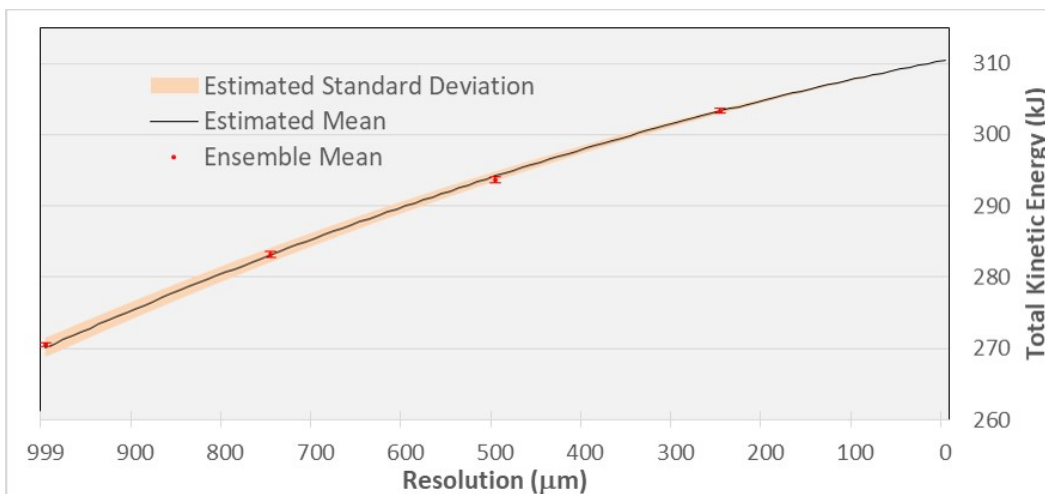


**Fig. 17** Estimated and ensemble values for total kinetic energy at 40  $\mu$ s vs. resolution

The relatively small inherent numerical variability makes it difficult to visually assess this plot. Subtracting the estimated mean from the data makes it easier to

compare estimated and measured distributions (Fig. 18). The estimated mean curve is now the plot axis, and the ensemble means are plotted relative to this. Distribution widths are better emphasized, with the estimated standard deviation represented by the shaded region and the ensemble standard deviations by error bars.

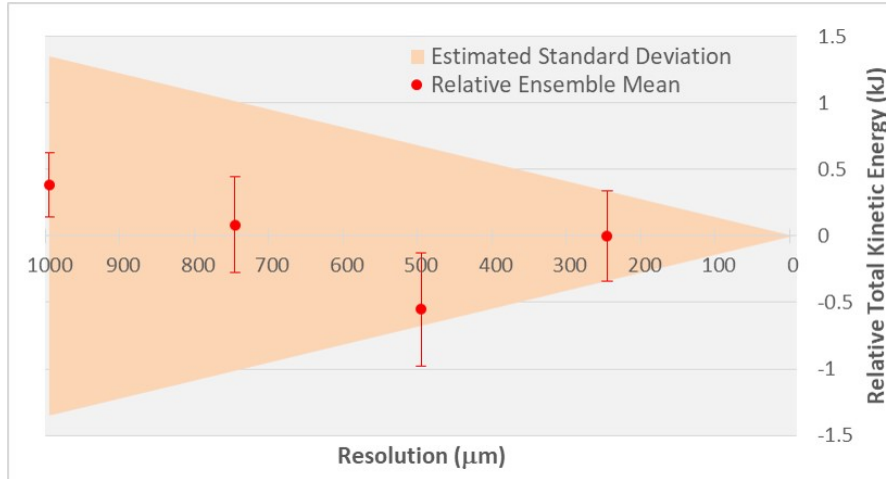


**Fig. 18 Ensemble values relative to estimated mean for total kinetic energy at 40  $\mu\text{s}$  vs. resolution**

The ensemble means are all nearly equal to the estimated means, with the largest difference of  $-0.56$  kJ at  $500\text{-}\mu\text{m}$  resolution being just  $0.2\%$  the size of the estimated mean. More interesting are the distribution widths, with estimated standard deviations outpacing measured values, especially at coarser resolution. Ensemble standard deviations actually decrease going from  $500\text{-}$  to  $999\text{-}\mu\text{m}$  resolution. To be clear, while the distribution of values narrows with increasing cell size, the mean value continues to move farther from the continuum limit estimate. Simulations at coarser resolution remain less-accurate approximations of the continuum system; they just return a smaller range of less-accurate values.

As discussed in the previous report, variability is expected to decrease as resolution goes to zero. This should not be taken to imply that variability will strictly increase as cell size increases. It may be the case, for instance, that variability also correlates with the number of domain cells, so that significantly reducing the number of elements in a domain tempers variability. If such an effect exists, uncertainty estimates could be improved by accounting for it.

Relative value plots can be generated for the other jet properties. Total axial momentum (Fig. 19) has much the same character as total kinetic energy, with ensemble means closely following the estimated values and ensemble distributions narrowing as cell size increases from  $500$  to  $999\text{ }\mu\text{m}$ .

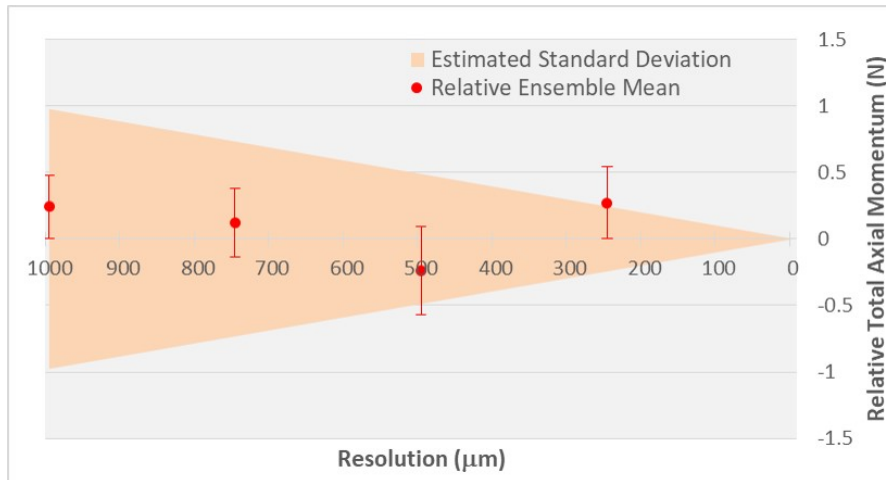


**Fig. 19** Ensemble values relative to estimated mean for total kinetic energy at 40  $\mu\text{s}$  vs. resolution

Mass average temperature (Fig. 20) presents a somewhat different picture. The ensemble means remain in good agreement with the estimates, with the largest difference of 7.2 K at 999- $\mu\text{m}$  resolution being just 0.7% the size of the estimated mean. However, ensemble standard deviations are significantly narrower than estimated distribution widths, and become progressively larger with increasing cell size across the entire range of the data.

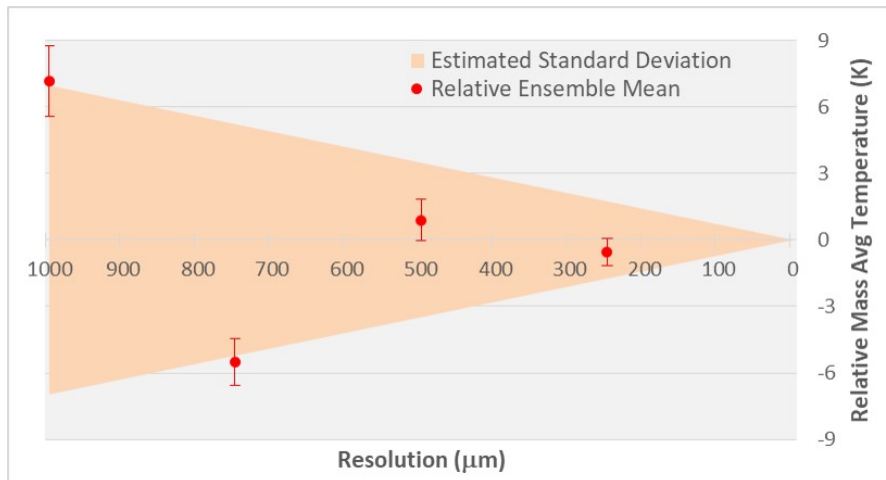


**Fig. 20** Ensemble values relative to estimated mean for total kinetic energy at 40  $\mu\text{s}$  vs. resolution

Total internal energy (Fig. 21) exhibits the same progressively increasing ensemble width, but the estimated standard deviations do not outpace ensemble values quite as much as for mass average temperature.

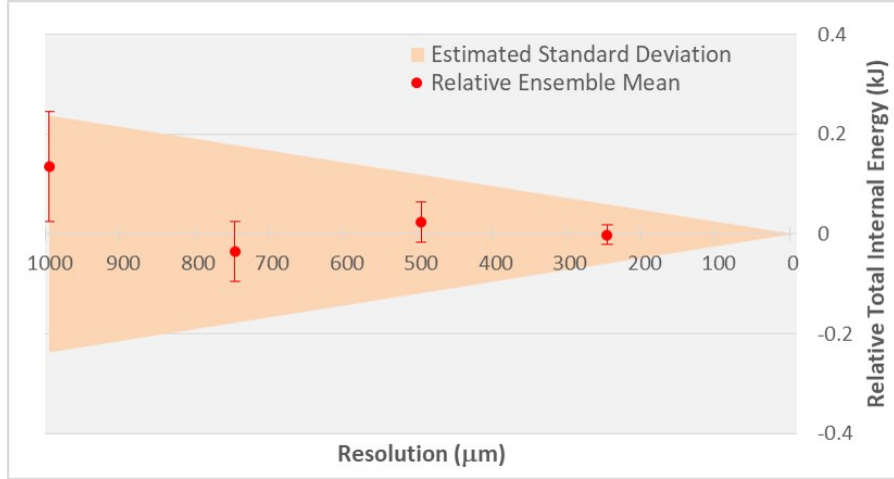


**Fig. 21 Ensemble values relative to estimated mean for total kinetic energy at 40  $\mu$ s vs. resolution**

The data in Figs. 19–21 are summarized numerically in Table 2. Overall, the estimated mean values quite accurately predict the resulting ensemble means. Estimated standard deviations tend to overshoot actual ensemble distribution widths, especially at coarse resolutions, typically by a factor of 3–5. Still, for an ad hoc method built on expedient statistical assumptions, the estimated standard deviations are not entirely detached from the observed results and serve as a useful upper bound on the inherent numerical uncertainty for this model system.

**Table 2 Comparison of estimated and ensemble mean values and standard deviations for jet properties at 40  $\mu$ s across multiple resolutions**

Jet property at 40 $\mu$ s		999 $\mu$ m		750 $\mu$ m		500 $\mu$ m		250 $\mu$ m	
		Mean	$\sigma$	Mean	$\sigma$	Mean	$\sigma$	Mean	$\sigma$
Total kinetic energy (kJ)	Estimated	270.2	1.35	283.1	1.01	294.2	0.68	303.3	0.34
	Ensemble	270.6	0.24	283.2	0.36	293.6	0.43	303.6	0.30
Total axial momentum (N)	Estimated	131.7	0.98	132.5	0.73	132.6	0.49	132.1	0.24
	Ensemble	131.9	0.24	132.6	0.26	132.4	0.33	132.4	0.27
Mass average temperature (K)	Estimated	1009.2	6.96	897.9	5.22	808.9	3.48	742.7	1.74
	Ensemble	1016.4	1.59	892.4	1.07	809.8	0.95	742.2	0.62
Total internal energy (kJ)	Estimated	32.8	0.24	29.0	0.18	26.1	0.12	23.9	0.06
	Ensemble	32.9	0.11	29.0	0.06	26.1	0.04	23.9	0.02

## 5. Conclusion

---

This report follows up on three open questions from previous work: 1) what is the underlying cause of the fragmented jet-tip morphology at high resolution, 2) how does the thermodynamic state of the pressure head vary with temporal discretization, and 3) how accurate are the estimates for resolution-dependent numerical uncertainty?

Fragmentation of the jet tip has been shown to be driven by the void insertion model, with the threshold fracture pressure determining the onset of voids along the jet axis. Data suggest that the fragmented morphology may be a transient phenomenon with respect to resolution, with the jet returning to a solid structure as cell size continues to decrease toward zero.

Limiting the duration of time steps at fixed resolution was shown to increase the mass average temperature of a jet. It follows that the general decrease of jet temperature with decreasing cell size must be driven by spatially related effects that surpass temporal ones.

Finally, 2-D ensembles of randomized simulations at multiple resolutions show that the estimated resolution-dependent standard deviations tend to be much larger than actual ensemble widths, and the estimation method as currently formulated is best taken as producing upper-bound estimates for the numerical uncertainty.

## 6. References

---

---

1. Hornbaker DJ. Resolution as a computational factor in ALEGRA simulations of a shaped-charge jet. Aberdeen Proving Ground (MD): CCDC Army Research Laboratory (US); 2020 May. Report No.: ARL-TR-8954.
2. Doney RL, Niederhaus JHJ, Fuller TJ, Coppinger MJ. Effects of EOS and constitutive models on simulating copper shaped charge jets in ALEGRA. *International Journal of Impact Engineering*. 2020;136:103428.
3. Doney R. Simulations predicting the effects of detonation velocity on the speed and temperature of shaped charge jets. Aberdeen Proving Ground (MD): CCDC Army Research Laboratory (US); 2020 June. Report No.: ARL-TR-8972.
4. Kmetyk LN, Yarrington P, Vigil MG. CTH analyses of Viper conical shaped charges with comparisons to experimental data. Albuquerque (NM): Sandia National Laboratories; 1991 Jan. Report No.: SAND90-2604.
5. Niederhaus JHJ, Uhlig WC. Analysis and validation for shaped charge jet simulations using ALEGRA. Albuquerque (NM): Sandia National Laboratories; 2011 Apr. Report No.: SAND2011-2819.
6. Matsumoto M, Nishimura T. Mersenne Twister: a 623-dimensionally equidistributed uniform pseudorandom number generator. *ACM Transactions on Modeling and Computer Simulation*. 1998;8(1):3–30.
7. Stephens MA. EDF statistics for goodness of fit and some comparisons. *Journal of the American Statistical Association*. 1974;69:730–737.

## **Appendix A. Randomly Generated Parameter Values for Simulation Ensembles**

---

---

Tables of randomly generated parameter values for the simulation ensembles in Section 4 of the main report are provided. Parameter lists were manually reviewed after generation to ensure there were no duplicate simulations. Estimating the probability of randomly generating duplicates is a useful exercise.

Duplicate outcomes will be most likely when the number of unique possibilities is smallest. In this report, this corresponds to the ensemble at 999- $\mu\text{m}$  resolution with unrestricted maximum time steps, which has four randomized factors with ranges of 26, 26, 26 and 999 possible values, for 17,558,424 unique combinations of parameter values.

Estimating the chance of a duplicate outcome is a generalization of the ‘‘Birthday Problem’’, typically posed as the probability that in a group of  $n$  people at least two have the same birthday. The simplest approach to a solution is to consider the complementary problem: What is the likelihood that every outcome (person) has a unique value (birthday)? For the general case of  $n$  selections from  $k$  values ( $k = 365$  for the Birthday Problem), the probability  $P$  is

$$P(n, k) = 1 - \frac{k!}{k^n (k-n)!} \quad (\text{A-1})$$

The large factorial terms call for Stirling’s approximation,

$$x! \sim \sqrt{2\pi x} \left(\frac{x}{e}\right)^x \quad (\text{A-2})$$

Substituting and simplifying,

$$P(n, k) \sim 1 - \frac{1}{e^n} \left(\frac{k}{k-n}\right)^{(k-n+1/2)} \quad (\text{A-3})$$

For  $n = 100$  and  $k = 17,558,424$ , the estimated probability of at least one duplicate value is  $P \approx 0.028\%$ . Stated another way, the expected rate at which duplication should occur is about once in every 3,548 ensembles of 100 samples.

Table A-1 lists the parameter values for the 500- $\mu\text{m}$  resolution ensemble discussed in Section 4.2 of the main report.

**Table A-1 Randomized parameter values for the 500- $\mu\text{m}$ -resolution simulation ensemble**

Added radial cells	Added axial cells		Origin shift ( $\mu\text{m}$ )	Max time step (ns)
	Negative	Positive		
47	23	30	100	8
17	18	21	86	34
19	23	27	445	23
39	39	41	445	11
41	29	1	395	24
31	26	0	233	3
9	3	23	137	42
15	20	41	411	18
50	5	50	285	17
1	49	40	315	38
42	43	7	190	28
35	38	11	188	19
23	41	1	414	33
21	29	33	499	27
18	50	9	485	33
38	34	48	437	14
47	44	35	250	19
22	13	15	366	32
2	44	36	408	20
50	13	28	298	45
6	39	23	162	16
43	48	50	0	39
13	22	6	0	32
4	36	34	380	43
34	19	46	224	31
24	43	34	334	29
30	18	8	97	2
35	2	14	357	11
42	2	24	409	38
49	32	4	67	1
27	35	11	403	3
44	12	38	84	24
18	3	19	303	7
16	3	45	414	20
6	1	14	330	8
5	32	30	282	16
16	4	44	60	35
46	25	47	175	37
38	3	31	474	15

**Table A-1 Randomized parameter values for the 500- $\mu\text{m}$ -resolution simulation ensemble (continued)**

Added radial cells	Added axial cells		Origin shift ( $\mu\text{m}$ )	Max time step (ns)
	Negative	Positive		
47	23	18	138	7
35	5	47	274	27
39	16	1	112	15
28	17	13	165	2
26	0	20	462	5
21	2	33	122	9
34	0	47	59	5
13	32	38	238	25
20	47	41	322	40
30	31	2	251	35
31	14	7	340	10
45	22	40	115	9
49	42	3	252	41
45	4	2	161	42
10	5	2	356	3
1	50	38	13	26
30	12	12	152	26
24	46	41	319	29
9	15	11	130	31
14	21	23	476	33
11	16	13	42	44
48	50	2	264	15
38	7	1	335	2
45	36	49	366	12
11	22	0	346	15
5	45	39	178	12
6	31	30	188	28
27	28	25	252	25
14	22	11	297	32
5	26	6	72	22
38	33	3	291	33
5	19	34	412	21
41	18	30	452	16
34	6	47	70	13
44	23	2	225	25
30	28	27	8	44
48	45	5	311	45
30	47	44	412	38

**Table A-1 Randomized parameter values for the 500- $\mu\text{m}$ -resolution simulation ensemble (continued)**

Added radial cells	Added axial cells		Origin shift ( $\mu\text{m}$ )	Max time step (ns)
	Negative	Positive		
44	25	7	311	35
42	18	32	282	46
23	38	8	176	16
49	44	23	460	29
5	47	46	269	2
5	11	46	6	24
8	39	5	7	37
30	10	14	387	45
12	8	12	139	12
16	40	21	410	12
13	26	1	477	11
21	43	36	365	34
50	9	5	332	42
35	44	37	94	30
40	8	35	46	9
41	32	29	138	19
14	0	4	222	24
11	10	31	55	10
39	22	7	231	8
2	32	7	54	5
34	7	44	421	31
23	29	12	103	43
28	8	13	2	45

Table A-2 lists the parameter values for the 500- $\mu\text{m}$ -resolution ensemble with unrestricted time steps discussed in Section 4.3 of the main report.

**Table A-2 Randomized parameter values for the 500- $\mu\text{m}$ -resolution simulation ensemble with unrestricted time steps**

Added radial cells	Added axial cells		Origin shift ( $\mu\text{m}$ )	Added radial cells	Added axial cells		Origin shift ( $\mu\text{m}$ )
	Negative	Positive			Negative	Positive	
36	40	40	184	45	8	46	296
11	0	20	74	36	28	5	80
42	45	38	420	12	34	50	267
41	46	26	135	42	36	37	113
38	42	36	414	6	32	49	376
35	32	8	91	7	29	25	398
7	3	42	40	11	22	24	355
1	13	20	253	47	9	44	466
43	36	7	439	27	35	38	422
34	33	10	109	29	12	35	216
23	14	14	151	12	21	26	132
8	12	12	185	31	40	38	179
42	27	50	168	19	25	10	402
14	37	44	279	46	50	15	124
23	8	19	138	17	25	25	180
9	15	48	263	8	29	36	480
39	7	5	83	43	32	18	356
31	23	35	32	36	23	16	460
33	12	28	42	32	6	25	132
48	43	21	174	24	18	49	397
25	45	25	61	47	16	47	201
28	20	31	129	11	19	45	257
16	40	24	241	19	25	20	249
12	49	29	54	43	43	17	425
11	16	13	257	27	49	7	411
30	34	43	352	18	29	42	290
6	16	42	159	12	39	0	407
44	7	29	321	42	18	1	123
10	8	34	108	22	10	43	485
21	50	3	413	10	30	6	50
29	3	48	246	48	39	41	183
4	13	42	168	39	0	16	53
29	12	27	227	27	33	34	481
48	14	2	114	26	3	8	0
23	12	48	107	8	41	4	369
0	34	20	334	39	9	4	0
48	17	24	470	3	5	2	499
38	14	27	445	8	46	45	350

**Table A-2 Randomized parameter values for the 500- $\mu\text{m}$ -resolution simulation ensemble with unrestricted time steps (continued)**

Added radial cells	Added axial cells		Origin shift ( $\mu\text{m}$ )	Added radial cells	Added axial cells		Origin shift ( $\mu\text{m}$ )
	Negative	Positive			Negative	Positive	
29	37	35	0	22	25	25	454
48	38	42	111	16	14	45	488
0	19	7	470	21	39	13	235
20	45	24	402	38	44	31	387
50	2	50	80	41	39	6	458
42	44	46	441	6	40	48	192
21	14	30	281	46	10	31	486
21	35	50	130	31	8	11	146
0	34	45	379	33	48	32	78
36	47	23	146	10	18	33	350
41	7	12	170	3	6	9	83
10	16	26	427	0	15	18	243

Table A-3 lists the parameter values for the 999- $\mu\text{m}$ -resolution ensemble with unrestricted time steps discussed in Section 4.4 of the main report.

**Table A-3 Randomized parameter values for the 999- $\mu\text{m}$ -resolution simulation ensemble with unrestricted time steps**

Added radial cells	Added axial cells		Origin shift ( $\mu\text{m}$ )	Added radial cells	Added axial cells		Origin shift ( $\mu\text{m}$ )
	Negative	Positive			Negative	Positive	
5	9	19	354	25	4	1	156
16	16	10	144	25	19	17	448
23	6	7	930	0	3	6	280
25	12	7	397	3	13	4	618
2	6	25	886	21	8	21	728
15	10	25	799	23	24	6	366
3	9	11	271	1	2	12	519
7	2	14	531	7	8	0	90
0	17	22	886	5	7	15	877
13	14	24	697	19	17	18	938
10	18	22	229	18	9	0	544
14	10	9	600	20	19	1	47
6	0	12	472	21	15	17	960
2	22	18	556	8	7	6	829
5	14	9	463	3	0	14	559
17	16	10	861	24	14	0	801
9	8	3	412	25	25	18	373
20	18	15	182	25	6	15	355
19	12	19	28	5	6	12	412
2	24	22	671	14	1	21	748
22	16	17	754	7	15	0	619
14	23	7	205	6	17	14	100
1	24	6	106	13	13	2	714
8	17	25	661	4	7	22	339
1	10	9	863	12	19	1	187
23	20	20	538	11	15	8	358
16	16	12	222	21	15	8	909
19	1	24	665	2	1	13	77
7	23	22	51	6	19	9	81
0	11	8	434	3	21	0	783
22	2	0	718	15	2	2	529
20	7	2	219	10	18	13	156
2	19	14	338	4	12	18	615
6	18	17	111	12	3	15	207
18	7	9	699	4	8	24	32
24	24	1	935	17	12	12	8
12	10	11	876	20	17	10	804
4	19	17	116	18	3	9	193

**Table A-3 Randomized parameter values for the 999- $\mu\text{m}$ -resolution simulation ensemble with unrestricted time steps (continued)**

Added radial cells	Added axial cells		Origin shift ( $\mu\text{m}$ )	Added radial cells	Added axial cells		Origin shift ( $\mu\text{m}$ )
	Negative	Positive			Negative	Positive	
24	15	14	564	13	23	7	832
11	12	10	117	2	14	19	358
20	5	20	849	14	0	1	709
18	6	15	505	4	9	0	326
3	1	12	247	9	19	10	67
13	21	22	704	1	20	13	904
6	8	14	220	21	3	5	953
4	3	5	76	0	8	4	123
10	9	8	39	1	15	17	804
24	7	19	615	21	13	12	355
4	18	21	159	24	15	14	273
16	18	22	897	1	22	19	98

Table A-4 lists the parameter values for the 750- $\mu\text{m}$ -resolution ensemble with unrestricted time steps discussed in Section 4.4 of the main report.

**Table A-4 Randomized parameter values for the 750- $\mu\text{m}$ -resolution simulation ensemble with unrestricted time steps**

Added radial cells	Added axial cells		Origin shift ( $\mu\text{m}$ )	Added radial cells	Added axial cells		Origin shift ( $\mu\text{m}$ )
	Negative	Positive			Negative	Positive	
36	40	40	184	36	40	40	184
11	0	20	74	11	0	20	74
42	45	38	420	42	45	38	420
41	46	26	135	41	46	26	135
38	42	36	414	38	42	36	414
35	32	8	91	35	32	8	91
7	3	42	40	7	3	42	40
1	13	20	253	1	13	20	253
43	36	7	439	43	36	7	439
34	33	10	109	34	33	10	109
23	14	14	151	23	14	14	151
8	12	12	185	8	12	12	185
42	27	50	168	42	27	50	168
14	37	44	279	14	37	44	279
23	8	19	138	23	8	19	138
9	15	48	263	9	15	48	263
39	7	5	83	39	7	5	83
31	23	35	32	31	23	35	32
33	12	28	42	33	12	28	42
48	43	21	174	48	43	21	174
25	45	25	61	25	45	25	61
28	20	31	129	28	20	31	129
16	40	24	241	16	40	24	241
12	49	29	54	12	49	29	54
11	16	13	257	11	16	13	257
30	34	43	352	30	34	43	352
6	16	42	159	6	16	42	159
44	7	29	321	44	7	29	321
10	8	34	108	10	8	34	108
21	50	3	413	21	50	3	413
29	3	48	246	29	3	48	246
4	13	42	168	4	13	42	168
29	12	27	227	29	12	27	227
48	14	2	114	48	14	2	114
23	12	48	107	23	12	48	107
0	34	20	334	0	34	20	334
48	17	24	470	48	17	24	470
38	14	27	445	38	14	27	445

**Table A-4 Randomized parameter values for the 750- $\mu\text{m}$ -resolution simulation ensemble with unrestricted time steps (continued)**

Added radial cells	Added axial cells		Origin shift ( $\mu\text{m}$ )	Added radial cells	Added axial cells		Origin shift ( $\mu\text{m}$ )
	Negative	Positive			Negative	Positive	
29	37	35	0	29	37	35	0
48	38	42	111	48	38	42	111
0	19	7	470	0	19	7	470
20	45	24	402	20	45	24	402
50	2	50	80	50	2	50	80
42	44	46	441	42	44	46	441
21	14	30	281	21	14	30	281
21	35	50	130	21	35	50	130
0	34	45	379	0	34	45	379
36	47	23	146	36	47	23	146
41	7	12	170	41	7	12	170
10	16	26	427	10	16	26	427

Table A-5 lists the parameter values for the 250- $\mu\text{m}$ -resolution ensemble with unrestricted time steps discussed in Section 4.4 of the main report.

**Table A-5 Randomized parameter values for the 250- $\mu\text{m}$ -resolution simulation ensemble with unrestricted time steps**

Added radial cells	Added axial cells		Origin shift ( $\mu\text{m}$ )	Added radial cells	Added axial cells		Origin shift ( $\mu\text{m}$ )
	Negative	Positive			Negative	Positive	
39	25	32	169	11	92	36	63
12	88	78	66	59	25	74	142
53	69	22	181	37	35	55	21
48	62	68	5	24	50	8	104
46	37	25	219	45	63	59	142
2	33	94	170	16	71	67	63
68	55	69	66	35	94	87	0
43	10	60	232	53	20	99	13
56	8	42	52	95	81	40	146
40	72	37	150	97	16	47	180
50	79	74	83	25	44	15	49
8	3	93	202	79	76	10	178
77	15	22	139	87	8	65	72
21	15	57	101	51	55	99	149
56	78	93	132	88	4	93	220
35	77	85	39	43	28	2	218
4	64	89	33	81	4	16	81
65	83	55	1	12	28	21	184
34	89	57	86	75	76	86	103
20	99	69	59	69	80	100	169
46	91	65	213	47	17	98	231
46	3	3	122	32	90	15	182
62	69	50	74	82	80	85	12
73	3	33	231	27	61	33	65
39	63	73	61	19	72	48	52
80	57	78	45	68	74	81	208
50	62	56	213	32	17	53	58
58	28	50	110	80	82	8	143
10	75	61	130	96	26	74	180
100	39	29	108	7	9	60	229
93	75	39	16	32	6	100	214
55	67	34	214	52	45	99	217
59	10	54	107	6	68	90	56
44	41	20	147	85	96	26	63
6	21	28	39	56	43	10	218
89	69	48	98	3	42	17	195
49	42	32	54	98	37	56	159
20	98	44	226	0	3	90	92

**Table A-5 Randomized parameter values for the 250- $\mu\text{m}$ -resolution simulation ensemble with unrestricted time steps (continued)**

Added radial cells	Added axial cells		Origin shift ( $\mu\text{m}$ )	Added radial cells	Added axial cells		Origin shift ( $\mu\text{m}$ )
	Negative	Positive			Negative	Positive	
89	25	1	225	57	30	6	77
48	81	34	176	8	25	14	58
77	13	88	215	100	25	84	11
80	82	54	245	34	0	15	175
30	58	24	221	0	27	99	164
44	22	25	11	33	41	28	133
28	11	72	25	5	51	26	238
44	35	82	213	13	9	46	136
46	0	38	145	43	58	7	1
26	52	22	202	74	47	99	79
2	87	42	140	80	65	95	235
54	42	59	26	47	39	3	56

## List of Symbols, Abbreviations, and Acronyms

---

2-D	two-dimensional
3-D	three-dimensional
EOS	equation of state
SCJ	shaped charge jet

1 DEFENSE TECHNICAL  
(PDF) INFORMATION CTR  
DTIC OCA

1 CCDC ARL  
(PDF) FCDD RLD CL  
TECH LIB

1 CCDC ARL  
(PDF) FCDD RLW PE  
D HORNBAKER